IEEE Access
Multidisciplinary | Rapid Review | Open Access Journal

Received October 1, 2019, accepted October 17, 2019, date of publication October 29, 2019, date of current version November 14, 2019.

Digital Object Identifier 10.1109/ACCESS.2019.2950179

Fast and Accurate Temperature-Dependent Current Modeling of HBTs Using the Dimension Reduction Method

WENRUI HU[1], ANDONG HUANG[2], HAORUI LUO[2], AND YONG-XIN GUO[1,2], (Fellow, IEEE)
[1]Department of Electrical and Computer Engineering, National University of Singapore, Singapore 117576
[2]National University of Singapore Suzhou Research Institute, Suzhou 21512, China

Corresponding author: Yong-Xin Guo (yongxin.guo@nus.edu.sg)

This work was supported in part by the National Research Foundation (NRF), Prime Minister's Office Singapore, under Grant NRF-CRP17-2017-08, in part by the Natural Science Foundation of Jiangsu Province, China, under Grant BK20191184, and in part by the Suzhou Science and Technology Council, China, under Grant SYG201839.

ABSTRACT Empirical models have been widely and successfully used in device modeling in the past few decades. However, they are becoming increasingly intricate to accurately capture the complex thermal effects in semiconductor devices. Therefore, the aim of this work is to utilize a general dimension-reduction method to quickly and accurately construct large-signal models of semiconductor devices with consideration of thermal effects. In general, the junction voltage dimension is represented by empirical functions, whereas the junction temperature dimension is described by the first-order Taylor series approximation. The final analytical current model is a combination of two independent sets of empirical functions. These functions are constructed from pulsed I-V measurements at different ambient temperatures. The percentages of different components are controlled by the thermal level. Two commercial InGaP/GaAs heterojunction bipolar transistors are investigated to verify the effectiveness of this method. The large-signal models are implemented in Advanced Design System. Excellent agreement is achieved between measurement and simulation of the I-V characteristics, S-parameters, and power sweeps. The dimension reduction method is able to effectively reduce the number of equations and parameters because the temperature dimension is expanded by using a Taylor series. In addition, this method would be applied to the thermal modeling of various devices based on new materials or process technologies. Accordingly, the dimension reduction method is powerful and useful in fast and accurate thermal modeling of microwave semiconductor devices.

INDEX TERMS Ambient temperature, dimension reduction, empirical model, HBT, large-signal model, self-heating, Taylor series, thermal.

I. INTRODUCTION

Heterojunction bipolar transistors (HBTs) are playing a vital role in high-speed and power applications, such as ultrafast circuits, microwave systems, and so on [1]–[5]. Nevertheless, there is a significant increase in the temperature resulting from the power consumption of the semiconductor devices, especially when the devices operate at high current density points in high speed and high power applications or when the devices become thinner. These thermal effects will degrade the performance of the microwave devices. Subsequently, large-signal models that are capable of characterizing with great accuracy the thermal effects are important and significant for the successful and efficient microwave circuit and system designs [6]–[8].

In the last decades, empirical models for semiconductor devices have been widely and successfully used in industrial applications because of their robustness, great simulation accuracy, and high efficiency [9]–[13]. However, in order to accurately capture the thermal effects in semiconductor devices, the temperature scaling equations in empirical models become increasingly complicated, which unfortunately makes the modeling work quite intricate and time-consuming. In addition, too many empirical parameters in the model could lead to nonphysical and overfitting problems. It would be difficult to achieve good results beyond the measurement region, especially when limited data sets are used to construct the large-signal models. In comparison with

The associate editor coordinating the review of this manuscript and approving it for publication was Andrei Muller.

empirical models, physical models are originated from the device operation principle, and they contain more physical parameters and fewer fitting parameters [14]. However, the accuracy and convergence of physical models need to be improved at some operation regions. Therefore, some empirical models are added in physical models, and semi-physical or semi-empirical models are used for accurate modeling [15]. In this work, a simplified AgilentHBT (AHBT) model is used for large-signal modeling. The current and charge models are similar to those in HICUM and VBIC models. However, the dimension reduction method is utilized to simplify temperature scaling equations and decrease the number of related parameters. Complicated thermal effects in microwave semiconductor devices can be quickly and accurately modeled using this method [16]. The core of this method is that the independent variables of a high-dimensional function are classified into two parts, and then different dimensions are represented by using different methods. The dimensions with enough measurement data that can be easily modeled are described by empirical functions, whereas the dimensions with limited data that are difficult to handle are characterized by the Taylor expansion.

In comparison to the traditional empirical modeling, the dimension reduction method directly expands empirical current functions instead of temperature-dependent model parameters. The temperature scaling equations and parameters are no longer needed for the model construction because the temperature dimension is expanded using the Taylor series. Therefore, this method takes fewer model parameters and equations for the analytical large-signal model construction. Hence, utilizing this method to capture the thermal effects would effectively shorten the model design time. In addition, this method is able to be applied for the thermal modeling of various devices or circuits based on different semiconductor materials or process technologies, such as LDMOS, GaN HEMTs, and so on [17]. Subsequently, this method would be helpful in realizing the automatic parameter extraction and semiconductor device modeling in the future.

In this paper, the detailed theoretical analyses and the whole modeling procedure are provided. The general dimension reduction approach is illustrated in Section II. The temperature-dependent current model is derived in Section III. In addition, the extraction of bias-independent elements and nonlinear charge models are provided. In Section IV, for verification, the simulated and measured results are compared, including both small-signal and large-signal characteristics. Section V is the conclusion of this paper.

II. DIMENSION REDUCTION METHOD

To begin with, the independent variables of a function or a model are classified into two parts. The highly nonlinear independent variables are in one group, whereas the remaining dimensions that behave monotonic or quasi-linear in the region of interest are in another group. After the classification of variables is finished, the function is represented as

$$h(\boldsymbol{m},\boldsymbol{n}) = h(p_1, p_2, \cdots, p_M, q_1, q_2, \cdots, q_N) \tag{1}$$

where the vector $\boldsymbol{m}$ is M-dimensional ($\boldsymbol{m} = (p_1, p_2, \cdots, p_M)$) and the vector $\boldsymbol{n}$ is N-dimensional ($\boldsymbol{n} = (q_1, q_2, \cdots, q_N)$). The vector $\boldsymbol{m}$ related dimension is highly nonlinear, and it will be represented by physical or empirical functions. By contrast, the vector $\boldsymbol{n}$ related dimension is quasi-linear in the region of interest, and it will be described by Taylor series expansion.

Second, the vector $\boldsymbol{n}$ related dimension is expanded at a quiescent point by using the first-order Taylor series approximation. In most cases, the first-order or second-order Taylor series approximation is utilized because the vector related $\boldsymbol{n}$ dimension exhibits weak nonlinearity over the region of interest, such as the thermal or trapping effects [18]. After Taylor series expansion, the original function is well approximated, and it is given by

$$h(\boldsymbol{m},\boldsymbol{n}) \approx h(\boldsymbol{m},\boldsymbol{n})|_{\boldsymbol{n}=\boldsymbol{n}_1} + \nabla h(\boldsymbol{m},\boldsymbol{n})|_{\boldsymbol{n}=\boldsymbol{n}_1} \cdot (\boldsymbol{n}-\boldsymbol{n}_1)^T \tag{2}$$

$$\nabla h(\boldsymbol{m},\boldsymbol{n})|_{\boldsymbol{n}=\boldsymbol{n}_1} = \left.\frac{\partial h(\boldsymbol{m},\boldsymbol{n})}{\partial \boldsymbol{n}}\right|_{n=n_1} \tag{3}$$

where $\boldsymbol{n}_1$ is the expansion point. $h(\boldsymbol{m},\boldsymbol{n})|_{\boldsymbol{n}=\boldsymbol{n}_1}$ represents the relationship between the function h and the dimension $\boldsymbol{m}$ at the expansion point. It will be described by empirical functions because the state is known or fixed ($\boldsymbol{n} = \boldsymbol{n}_1$). $\nabla h(\boldsymbol{m},\boldsymbol{n})|_{\boldsymbol{n}=\boldsymbol{n}_1}$ denotes the Jacobian at the expansion point.

The final step in the dimension reduction process is to obtain the expression of the Jacobian at the expansion point. Once the Jacobian is determined, the dimension $\boldsymbol{n}$ is reduced, and the original function is simplified. In fact, the expression of the Jacobian can be obtained from several data sets at different states. At a given state ($\boldsymbol{n} = \boldsymbol{n}_k$), the function is expressed as $h(\boldsymbol{m},\boldsymbol{n})|_{\boldsymbol{n}=\boldsymbol{n}_k}$, where k is a positive integer. For convenience, $h(\boldsymbol{m},\boldsymbol{n})|_{\boldsymbol{n}=\boldsymbol{n}_k}$ is denoted as $h(\boldsymbol{m},\boldsymbol{n}_k)$. Then, according to (2), for $k = 2, 3, \cdots, K$, there are $K-1$ equations, and they are as follows:

$$h(\boldsymbol{m},\boldsymbol{n}_k) \approx h(\boldsymbol{m},\boldsymbol{n}_1) + \nabla h(\boldsymbol{m},\boldsymbol{n})|_{\boldsymbol{n}=\boldsymbol{n}_1} \cdot (\boldsymbol{n}_k - \boldsymbol{n}_1)^T \tag{4}$$

Rearranging (4) in vector form, we obtain

$$\boldsymbol{A} \cdot \left[\nabla h(\boldsymbol{m},\boldsymbol{n})|_{\boldsymbol{n}=\boldsymbol{n}_1}\right]^T = \boldsymbol{b} \tag{5}$$

where $\boldsymbol{A}$ is a $(K-1) \times N$ matrix and $\boldsymbol{b}$ is a vector with $K-1$ elements. The expressions are as follows:

$$\boldsymbol{A} = \begin{bmatrix} (\boldsymbol{n}_2 - \boldsymbol{n}_1) \\ (\boldsymbol{n}_3 - \boldsymbol{n}_1) \\ \vdots \\ (\boldsymbol{n}_K - \boldsymbol{n}_1) \end{bmatrix} \tag{6}$$

$$\boldsymbol{b} = \begin{bmatrix} h(\boldsymbol{m},\boldsymbol{n}_2) - h(\boldsymbol{m},\boldsymbol{n}_1) \\ h(\boldsymbol{m},\boldsymbol{n}_3) - h(\boldsymbol{m},\boldsymbol{n}_1) \\ \vdots \\ h(\boldsymbol{m},\boldsymbol{n}_k) - h(\boldsymbol{m},\boldsymbol{n}_1) \end{bmatrix} \tag{7}$$

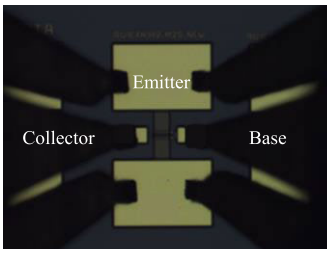

FIGURE 1. Microphotograph of the investigated InGaP/GaAs HBTs.

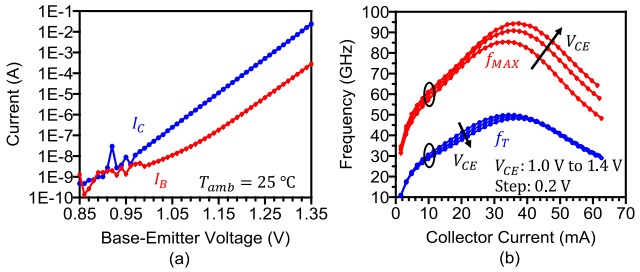

FIGURE 2. (a) Gummel plot and (b) f_T and f_{MAX} of the investigated HBT at room temperature. Arrows show the direction of change in V_{CE}.

Then the Jacobian can be uniquely determined from (5). If the number of the equations is the same as the dimension of the Jacobian, i.e., $K - 1 = N$, the Jacobian is determined by

$$\nabla h\,(\boldsymbol{m}, \boldsymbol{n})|_{\boldsymbol{n}=\boldsymbol{n}_1} = \left[\boldsymbol{A}^{-1} \cdot \boldsymbol{b}\right]^T \tag{8}$$

III. LARGE-SIGNAL MODELING OF HBTs

Two commercial 3 μm × 40 μm InGaP/GaAs HBTs are utilized to demonstrate how to use the dimension reduction method to model thermal effects. One HBT is 1-finger, and the other is 2-finger. Fig. 1 shows the microphotograph of the investigated InGaP/GaAs HBT device. Fig. 2(a) shows the measured current, cut-off frequency (f_T), and maximum frequency of oscillation (f_{MAX}) of the investigated 1-Finger HBT at room temperature. The f_T and f_{MAX} are nearly 50 GHz and 95 GHz at V_{CE} = 1.4 V and I_C = 35 mA. In addition, the collector-base, emitter-base, and 3 terminal emitter-collector junction breakdown voltages are nearly 25 V, 7 V, and 13 V, respectively (2 μm × 20 μm × 2 HBT at 40 μA). Fig. 3 illustrates the adopted nonlinear equivalent circuit of the investigated HBTs, which is made up of parasitic elements, resistors, current sources, etc. The intrinsic model is bounded by the red dashed box, and the thermal sub-circuit is bounded by the black dotted box. Fig. 4 demonstrates the detailed procedure for the parameter extraction and the nonlinear model construction.

A. BIAS-INDEPENDENT PARAMETER EXTRACTION

The parasitic capacitances (C_{pbe}, C_{pbc}, and C_{pce}) are extracted from the Y-parameter measurements of the open test structure. Similarly, the parasitic inductances (L_{pb}, L_{pc}, and L_{pe}) are determined by using the Z-parameters of the short test structure. The small contact resistances are taken into

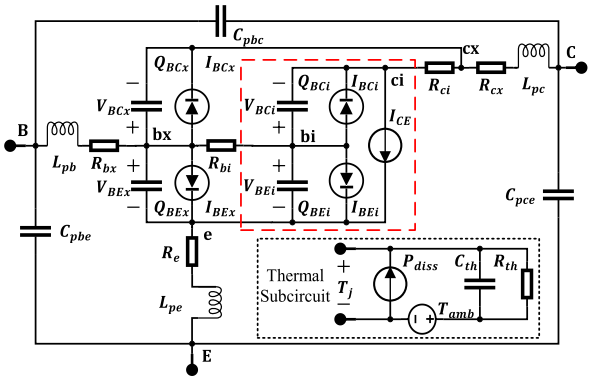

FIGURE 3. Topology of the large-signal model for the investigated InGaP/GaAs HBTs.

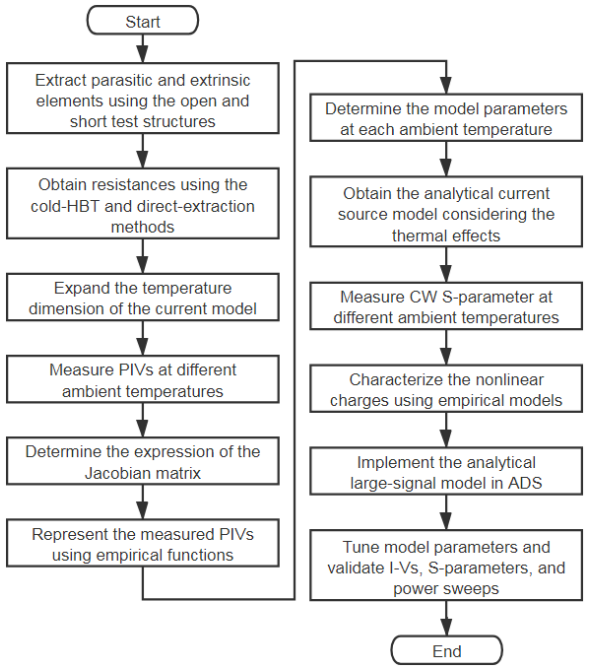

FIGURE 4. Design flow for the large-signal modeling of the 1-finger and 2-finger InGaP/GaAs HBTs.

consideration in the extrinsic base, extrinsic collector, and series emitter resistors, which are R_{bx}, R_{cx}, and R_e, respectively. These resistances are obtained by using the cold HBT method and the Z parameter method [19]–[22]. The intrinsic base resistance (R_{bi}) and collector resistance (R_{ci}) are determined from the measured S-parameters after all parasitic and extrinsic components are de-embedded [23]–[27].

Note that the base resistance affects the device speed and noise behavior, and it is important for the transistors operated at high current densities [28]. In addition, R_{bi} reduces with collector current due to current crowding effects [29]. In this work, the intrinsic base resistance is assumed to be bias-independent, which might affect the simulated f_{MAX}, S-parameters, and output power under high bias conditions. The extracted parameters of 1-finger and 2-finger HBTs are listed in Tables 1 and 2, respectively.

TABLE 1. Extracted Bias-Independent Parameters of the 1-Finger HBT.

C_{pbe}(fF)	C_{pce}(fF)	C_{pbc}(fF)	L_{pb}(pH)	L_{pc}(pH)	L_{pe}(pH)
18.6953	31.8424	2.038	48.4501	35.5578	2.7367
$R_{bi}(\Omega)$	$R_{bx}(\Omega)$	$R_{ci}(\Omega)$	$R_{cx}(\Omega)$	$R_e(\Omega)$	
5.203	1.8	0.05	1.1525	0.49	

TABLE 2. Extracted Bias-Independent Parameters of the 2-Finger HBT.

C_{pbe}(fF)	C_{pce}(fF)	C_{pbc}(fF)	L_{pb}(pH)	L_{pc}(pH)	L_{pe}(pH)
37.3906	57.76	3.057	46.5121	40.25	3.55
$R_{bi}(\Omega)$	$R_{bx}(\Omega)$	$R_{ci}(\Omega)$	$R_{cx}(\Omega)$	$R_e(\Omega)$	
3.63	0.792	0.05	1.05	0.49	

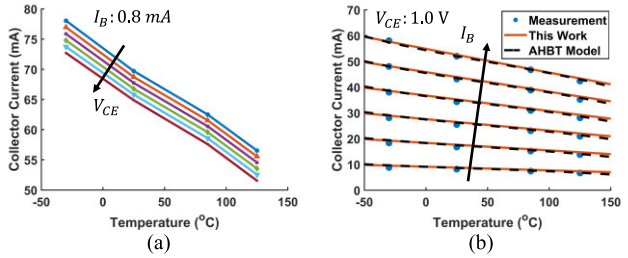

FIGURE 5. (a) Measured I_C with V_{CE} from 1.0 V to 2.25 V, and (b) measured and modeled I_C with I_B from 0.1 mA to 0.6 mA at different ambient temperatures.

B. TEMPERATURE-DEPENDENT CURRENT MODEL

The collector-emitter current (I_{CE}), base-collector currents (I_{BCx} and I_{BCi}), and base-emitter currents (I_{BEx} and I_{BEi}) are dependent on the junction voltages and junction temperature. The junction voltage dimension is highly nonlinear, and thus it is described by empirical functions instead of high-order Taylor series to avoid extrapolation problems. In contrast, the junction temperature dimension tends to behave quasi-linear or monotonic in the region of interest. Therefore, it is characterized by the Taylor series to reduce the number of parameters and simplify the modeling work. The first-order Taylor approximation is able to meet the engineering requirements in terms of prediction precision because there is a quasi-linear decrease of the current with the increase of the temperature over the region of interest [30]. Fig. 5 shows that the collector current decreases almost linearly with ambient temperature. In addition, a good agreement is achieved between the measured and modeled results in the region of interest. Therefore, the first-order approximation is adequate, and it is utilized in this work. A second- or higher-order approximation is needed if characteristics at much higher or lower temperatures are investigated.

According to the analyses in Section II, the variables are first classified into two parts as follows:

$$\boldsymbol{m} = \boldsymbol{V_j} = (V_{BCx}, V_{BCi}, V_{BEx}, V_{BEi}) \tag{9}$$

$$n = T_{dev} = T_{amb} + R_{th} \times P_{diss} \tag{10}$$

where V_{BCx}, V_{BCi}, V_{BEx}, and V_{BEi} are junction voltages. T_{dev} represents the junction temperature. T_{amb} is the ambient temperature, R_{th} denotes the thermal resistance, and P_{diss} is the average dissipated power. In this case, the vector $\boldsymbol{n}$ becomes a scalar because only T_{dev} will be expanded.

TABLE 3. Pulsed I-V Measurement Setup.

PIVs	T_{amb}(°C)	P_{diss}(W)	T_{dev}(°C)	n(°C)
$I(\boldsymbol{m}, n_1)$	25	≈ 0	≈ 25	$n_1 \approx 25$
$I(\boldsymbol{m}, n_2)$	125	≈ 0	≈ 125	$n_2 \approx 125$

Then the current source is represented by

$$I(\boldsymbol{m}, n) = I(V_{BCx}, V_{BCi}, V_{BEx}, V_{BEi}, T) \tag{11}$$

Applying the Taylor series expansion illustrated in (2), the current function is approximately expressed, which is given by

$$I(\boldsymbol{m}, n) \approx I(\boldsymbol{m}, n)|_{n=n_1} + \nabla I(\boldsymbol{m}, n)|_{n=n_1} \cdot (n - n_1)^T \tag{12}$$

where n_1 is the quiescent expansion point and $\nabla I(\boldsymbol{m}, n)|_{n=n_1}$ denotes the Jacobian at the expansion point.

In addition, according to (4), at different thermal states $n_k = T_{dev}^{(k)}$, $k = 1, 2, \cdots, K$, the current is expressed as follows:

$$I(\boldsymbol{m}, n_k) \approx I(\boldsymbol{m}, n_1) + \nabla I(\boldsymbol{m}, n)|_{n=n_1} \cdot (n_k - n_1)^T \tag{13}$$

The dimension to be expanded is 1 in this work, and thus the Jacobian at the expansion point has the dimension of 1 by 1. Therefore, at least two different pulsed I-V measurements, including the data at the quiescent expansion point, are required to determine the expression of the Jacobian and then to finish the dimension reduction process. Hence, short-pulsed I-V measurements at two different ambient temperatures are used for model construction. The pulsed I-V measurement setup is listed in Table 3.

In general, using pulsed I-V curves to obtain the Jacobian is more of convenience than utilizing DC I-V curves, because the average dissipated power is low, and the self-heating effect is negligible in pulsed measurements. In this work, the ambient temperatures of 25°C and 125°C are used as the reference states, and the related pulsed I-V measurements are used for model construction. In fact, all pulsed I-V measurements at two or more arbitrary temperatures in the region of interest are able to be used to determine the expression of the Jacobian.

Substituting the measurement information in Table 3 into (6) and (7), we have

$$\boldsymbol{A} = [(\boldsymbol{n}_2 - \boldsymbol{n}_1)] = (n_2 - n_1) = 125 - 25 \tag{14}$$

$$\boldsymbol{b} = [h(\boldsymbol{m}, \boldsymbol{n}_2) - h(\boldsymbol{m}, \boldsymbol{n}_1)] = I(\boldsymbol{m}, n_2) - I(\boldsymbol{m}, n_1) \tag{15}$$

The number of equations equals the dimension of the Jacobian. Therefore, the expression of the Jacobian is obtained by substituting (14) and (15) into (8), and it is given by

$$\nabla I(\boldsymbol{m}, n)|_{n=n_1} = \left[\boldsymbol{A}^{-1} \cdot \boldsymbol{b}\right]^T = \frac{I(\boldsymbol{m}, n_2) - I(\boldsymbol{m}, n_1)}{125 - 25} \tag{16}$$

From (16), it is observed that the determined Jacobian is a linear combination of the I-V characteristics at different

thermal states (n_1 and n_2). Thus, the value of the Jacobian is able to be obtained after the pulsed I-V characteristics at these states are correctly modeled by empirical functions.

After the expression of the Jacobian is determined, the analytical current model with ambient temperature dependence is obtained by substituting (16) and the information in Table 3 into (12), which is given by

$$I(\boldsymbol{m}, n) \approx I(\boldsymbol{m}, n_1) + \frac{I(\boldsymbol{m}, n_2) - I(\boldsymbol{m}, n_1)}{125 - 25}(n - 25) \quad (17)$$

The next step for current source modeling is to determine the model parameter values in $I(\boldsymbol{m}, n_1)$ and $I(\boldsymbol{m}, n_2)$ by using the pulsed I-V measurements at 25°C and 125°C, respectively. In this work, the relationship between currents and junction voltages is described by the empirical functions in the AHBT model which is based on the UCSD model and the Gummel-Poon model [31]–[34]. The empirical functions are as follows [35]:

$$I_{CE} = \frac{I_s}{DD}\left(\exp\left(\frac{V_{BEi}}{V_T N_f}\right) - 1\right) - \frac{I_{sr}}{DD}\left(\exp\left(\frac{V_{BCi}}{V_T N_r}\right) - 1\right) \quad (18)$$

$$DD = q_b + \frac{I_s}{I_{sa}}\exp\left(\frac{V_{BEi}}{V_T N_a}\right) + \frac{I_s}{I_{sb}}\exp\left(\frac{V_{BCi}}{V_T N_b}\right) \quad (19)$$

$$q_b = \frac{1}{2}\left(1 - \frac{V_{BEi}}{V_{ar}} + \frac{V_{BCi}}{V_{af}}\right)^{-1} \times \left(1 + \sqrt{1 + \frac{4I_s}{I_k}\exp\left(\frac{V_{BEi}}{V_T N_f}\right)}\right) \quad (20)$$

$$I_{BC} = I_{srh}\left(\exp\left(\frac{V_{BCx}}{V_T N_{rh}}\right) - 1\right) + I_{sc}\left(\exp\left(\frac{V_{BCx}}{V_T N_c}\right) - 1\right) \quad (21)$$

$$\frac{I_{BCx}}{ABCX} = \frac{I_{BCi}}{(1 - ABCX)} = I_{BC} \quad (22)$$

$$I_{BE} = I_{sh}\left(\exp\left(\frac{V_{BEx}}{V_T N_h}\right) - 1\right) + I_{se}\left(\exp\left(\frac{V_{BEx}}{V_T N_e}\right) - 1\right) \quad (23)$$

$$\frac{I_{BEx}}{ABEL} = \frac{I_{BEi}}{(1 - ABEL)} = I_{BE} \quad (24)$$

where $ABCX$ and $ABEL$ are utilized to separate the intrinsic and extrinsic current. V_T is the thermal voltage.

The parameters in the current model are determined by using the quasi-newton and least-square optimization methods to closely fit the pulsed I-V measurement at ambient temperatures of 25°C and 125°C. The optimization is carried out by using the Plot Optimizer in Integrated Circuit Characterization and Analysis Program (IC-CAP) with a Verilog file defining the current model. Note that some model parameters are temperature-independent, and thus they are set to be the same at different temperatures. The obtained current model parameters for the 1-finger and 2-finger HBTs are listed in Tables 4 and 5, respectively.

Fig. 6 shows the mesh of the obtained Jacobian coefficient. Fig. 7 and Fig. 8 illustrate the comparison between the measured and simulated pulsed I-V curves under four

TABLE 4. Temperature-Dependent and Temperature-Independent Current Model Parameters of the Investigated 1-Finger HBT.

PIVs	$I_s(10^{-25}$ A)	V_{af}(V)	N_f	I_{sa}(A)	N_a
$I(\boldsymbol{m}, n_1)$	5.0242	1000	1.0053	10^9	2.0
$I(\boldsymbol{m}, n_2)$	5.0135	1000	1.0086	10^9	2.0
PIVs	$I_{sr}(10^{-25}$ A)	V_{ar}(V)	N_r	I_{sb}(A)	N_b
$I(\boldsymbol{m}, n_1)$	4.9378	1000	1.0068	10^9	2.0
$I(\boldsymbol{m}, n_2)$	4.7780	1000	0.9790	10^9	2.0
PIVs	$I_{srh}(10^{-20}$ A)	$I_{sh}(10^{-25}$ A)	N_{rh}	N_h	$ABCX$
$I(\boldsymbol{m}, n_1)$	95.0	0.15500	1.3475	1.0252	0.59
$I(\boldsymbol{m}, n_2)$	30.489	0.15567	1.3475	1.0252	0.59
PIVs	$I_{sc}(10^{-15}$ A)	$I_{se}(10^{-20}$ A)	N_c	N_e	$ABEL$
$I(\boldsymbol{m}, n_1)$	73.375	96.92	2.0357	2.0916	0.95
$I(\boldsymbol{m}, n_2)$	98.964	4.846	2.0357	2.0916	0.95
PIVs	I_k(A)				
$I(\boldsymbol{m}, n_1)$	10^6				
$I(\boldsymbol{m}, n_2)$	10^6				

TABLE 5. Temperature-Dependent and Temperature-Independent Current Model Parameters of the Investigated 2-Finger HBT.

PIVs	$I_s(10^{-25}$ A)	V_{af}(V)	N_f	I_{sa}(A)	N_a
$I(\boldsymbol{m}, n_1)$	6.944	1000.0	1.0065	2×10^9	2.0
$I(\boldsymbol{m}, n_2)$	6.901	1000.0	1.0095	2×10^9	2.0
PIVs	$I_{sr}(10^{-25}$ A)	V_{ar}(V)	N_r	I_{sb}(A)	N_b
$I(\boldsymbol{m}, n_1)$	23.778	1000.0	1.0061	2×10^9	2.0
$I(\boldsymbol{m}, n_2)$	23.731	1000.0	1.0002	2×10^9	2.0
PIVs	$I_{srh}(10^{-20}$ A)	$I_{sh}(10^{-25}$ A)	N_{rh}	N_h	$ABCX$
$I(\boldsymbol{m}, n_1)$	6.553	0.201	1.359	1.0252	0.59
$I(\boldsymbol{m}, n_2)$	6.531	0.206	1.359	1.0252	0.59
PIVs	$I_{sc}(10^{-15}$ A)	$I_{se}(10^{-20}$ A)	N_c	N_e	$ABEL$
$I(\boldsymbol{m}, n_1)$	87.383	8.275	2.0357	2.249	0.95
$I(\boldsymbol{m}, n_2)$	84.119	8.258	2.0357	2.249	0.95
PIVs	I_k(A)				
$I(\boldsymbol{m}, n_1)$	10^6				
$I(\boldsymbol{m}, n_2)$	10^6				

different temperatures. In fact, the pulsed I-V measurements at 25°C and 125°C are utilized for the curve fitting and model parameter determination. The good agreement shows that the model parameters are accurately determined by using optimization techniques. In addition, the designed current models are able to predict with great accuracy the pulsed I-V curves at −30°C and 85°C. The current correctly decreases with the increase of the ambient temperature under different bias conditions. Therefore, the effects of the ambient temperature on the HBTs are correctly characterized by using the dimension reduction method. The expansion is valid, and the convergence is guaranteed in a wide range of simulations.

The final step of the current modeling is to model the self-heating effect. Substituting (10) into (17), the below current model with consideration of thermal effects is obtained.

$$I(\boldsymbol{m}, n) \approx I(\boldsymbol{m}, n_1) + 0.01 \cdot [I(\boldsymbol{m}, n_2) - I(\boldsymbol{m}, n_1)] \cdot (T_{amb} + R_{th} \times P_{diss} - 25) \quad (25)$$

The average dissipated power equals the product of the collector-emitter voltage and the collector-emitter current. The model parameters in $I(\boldsymbol{m}, n_1)$ and $I(\boldsymbol{m}, n_2)$

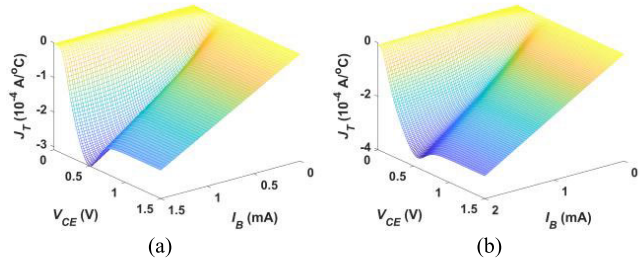

FIGURE 6. Mesh plots of the obtained Jacobian J_T for (a) 1-finger HBT with base current I_B from 0 mA to 1.5 mA; (b) 2-finger HBT with I_B from 0 mA to 2.0 mA. The collector voltage V_{CE} increases from 0 V to 1.5 V.

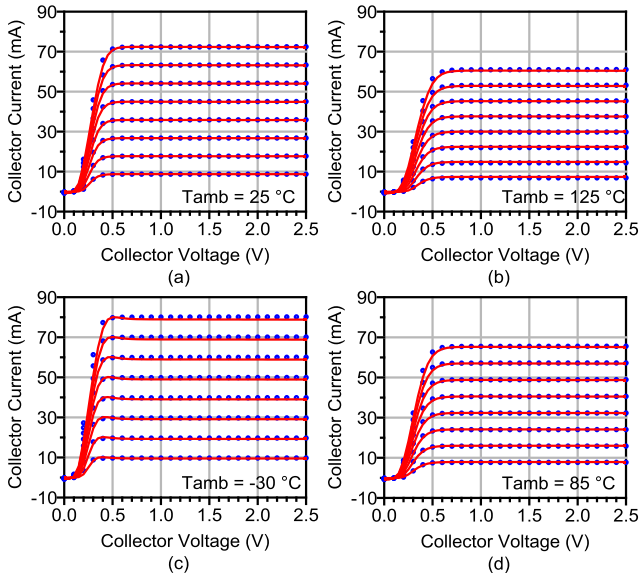

FIGURE 7. Measured (blue circles) and predicted (solid lines) PIVs by the analytical current model of the 1-finger HBT at different ambient temperature (a) $T_{amb} = 25°C$; (b) $T_{amb} = 125°C$; (c) $T_{amb} = -30°C$; (d) $T_{amb} = 85°C$. V_{CE} increases from 0 V to 2.5 V in increments of 0.05 V and I_B increases from 100 μA to 800 μA in increments of 100 μ A.

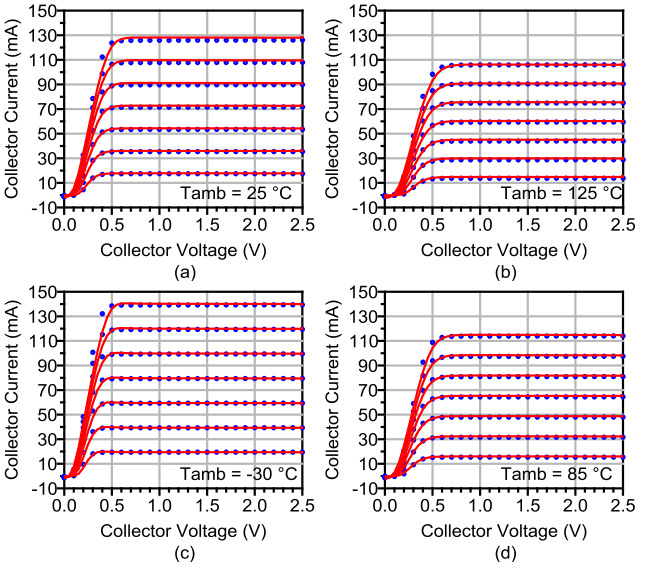

FIGURE 8. Measured (blue circles) and predicted (solid lines) PIVs by the analytical current model of the 2-finger HBT at different ambient temperature (a) $T_{amb} = 25°C$; (b) $T_{amb} = 125°C$; (c) $T_{amb} = -30°C$; (d) $T_{amb} = 85°C$. V_{CE} increases from 0 V to 2.5 V in increments of 0.05 V and I_B increases from 0.2 mA to 1.4 mA in increments of 0.2 mA.

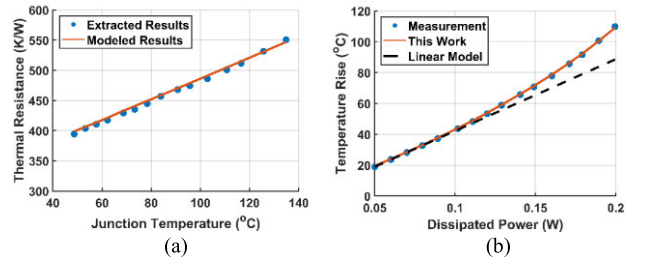

FIGURE 9. (a) Comparison between the extracted (symbols) and modeled (line) thermal resistances, and (b) comparison between the measurement (symbols), the linear model (dashed line), and this work's result (solid line). The ambient temperature is 25°C.

are determined in the previous optimization process. Therefore, the unknown model parameter in (25) is thermal resistance. It is significant to note that the thermal resistance also depends on the junction temperature, which is a vital property of III-V HBTs [36]–[38]. The thermal resistances at different states are obtained using the method in [39]. Fig. 9 (a) illustrates that R_{th} ranges from about 400 K/W at low power dissipation to 550 K/W at high power dissipation. The increase in R_{th} with an increase in temperature is due to the decreasing thermal conductivity with the temperature. It means the assumption of constant thermal conductivity may not hold [40]. As shown in Fig. 9 (b), the nonlinearity occurs at high power dissipation. The linear model (black dashed line) assuming constant thermal conductivity underestimates the temperature rise when the power dissipation is higher than 0.1 W. Therefore, the temperature dependence of thermal conductivity is considered in this work, and temperature-dependent thermal resistance is modeled by

$$R_{th} = R_{thref} \times \left(\frac{273.15 + T_{dev}}{273.15 + T_{nom}} \right)^{X_{th}} \tag{26}$$

where T_{nom} is the nominal temperature, and it is 27°C. R_{thref} is obtained from the experimental data at low power dissipation. X_{th} is the temperature exponent, and it is obtained by fitting the extracted thermal resistances at different thermal states. Fig. 9 (a) shows that a good agreement is achieved between the extracted and modeled thermal resistances, and Fig. 9 (b) shows that the nonlinear temperature rise is correctly modeled.

The thermal time constant (τ_{th}) and thermal capacitance (C_{th}) are obtained from the pulsed I-V measurements with different pulse widths. First, τ_{th} that indicates a time for a transistor to respond to a change is extracted from the graph of normalized difference unit (NDU) versus pulse length [41]. Fig. 10 shows that the estimated thermal time constant is approximately 819 ns when approximately 63.2 percent ($\left(1 - e^{-1}\right) \times 100\%$) of the resulting change in the junction temperature has occurred. After τ_{th} is determined, C_{th} is assumed to be temperature-independent, and it is obtained by

$$C_{th} = \frac{\tau_{th}}{R_{thref}} \tag{27}$$

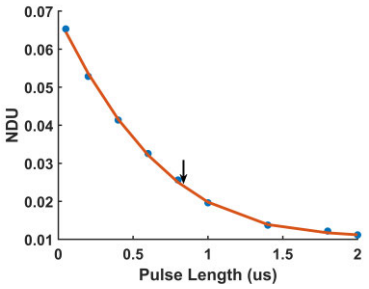

FIGURE 10. Extraction of the thermal time constant from the graph of NDU versus pulse length.

TABLE 6. Extracted Thermal Resistances and Capacitances of the Investigated 1-Finger and 2-Finger HBTs.

	R_{thref} (K/W)	C_{th} (J/K)	X_{th}
1-Finger	364.71	2.24×10^{-9}	1.32
2-Finger	335.56	3.02×10^{-9}	1.26

The determined values of thermal resistances and capacitances are listed in Table 6.

In this work, the temperature scaling equations and corresponding parameters are no longer needed for the model construction, because the temperature-related dimension is expanded using the first-order Taylor series approximation. As a result, the number of model parameters is reduced by 12 in comparison to the AHBT current model [35]. In addition, thermal modeling based on the dimension reduction method is analytical without any optimization. In the current model construction process, optimization is only used to fit the pulsed I-V curves at each ambient temperature. In each optimization process, the temperature variable in the empirical functions is fixed, and it equals 25°C or 125°C. In other words, the empirical functions only have the junction voltage dimension. In contrast, the conventional methods have to handle two dimensions including both the junction voltage dimension and the device temperature dimension in the optimization process.

A scalable model is very important for circuit design. According to the analyses in [42] and [43], the emitter dimension (emitter length L_e or emitter area A_e) could be added into the dimensions to be expanded. Then, the current is approximately expressed by using (2). For example, the vector $\boldsymbol{n}$ is assumed to be (T_{dev}, L_e) and thus, the Jacobian has the dimension of 1-by-2. Therefore, at least three different reference states are required to obtain the Jacobian (using (8)). The related pulsed I-V measurements are used to obtain all the parameters in the current model. Further studies are required.

C. NONLINEAR CHARGE SOURCE MODEL

Depletion and diffusion charge models are considered to build nonlinear charge models. The base-collector or base-emitter depletion charge models comprise four terms, which are Q_{jXf}, Q_{jXm}, Q_{jXr}, and Q_{jXcorr}. The variable X represents either base-to-emitter or base-to-collector and V_X denotes the related junction voltage. The functions are as follows [44]:

$$Q_{Xd}(V_X) = Q_{jXf} + Q_{jXm} + Q_{jXr} - Q_{jXcorr} \tag{28}$$

$$Q_{jXf} = C_{Xmax}\left(V_X - v_{jXr}\right) \tag{29}$$

$$Q_{jXm} = C_{jX} V_{jX}\left(M_{jXr} - 1\right)^{-1}\left(1 - v_{jXm}/V_{jX}\right)^{1-M_{jX}} \tag{30}$$

$$Q_{jXr} = C_{jX} V_{jX}\left(M_{jXr} - 1\right)^{-1}\left(1 - v_{jXr}/V_{jX}\right)^{1-M_{jXr}} \tag{31}$$

$$Q_{jXcorr} = C_{jX} V_{jX}\left(M_{jXr} - 1\right)^{-1}\left(1 - v_{jXm}/V_{jX}\right)^{1-M_{jXr}} \tag{32}$$

$$v_{jXm} = 0.5\left[v_{jXr} - V_{jpXi} + \sqrt{\left(V_{jpXi} + v_{jXr}\right)^2 + V_{rX}^2}\right] \tag{33}$$

$$V_{rX} = 0.1 V_{jpXi} + 4kT/q \tag{34}$$

$$v_{jXr} = 0.5\left[V_X + V_{fXi} - \sqrt{\left(V_{fXi} - V_X\right)^2 + (kT/q)^2}\right] \tag{35}$$

$$V_{jpXi} = V_{ptX} - V_{jX} \tag{36}$$

$$V_{fXi} = V_{jX}\left[1 - \left(C_{Xmax}/C_{jX}\right)^{-1/M_{jX}}\right] \tag{37}$$

The diffusion charges exist only in the intrinsic region, which is different from the depletion charges, because they describe the traverse time along the intrinsic region [45], [46]. The equations are as follows [47], [48]:

$$Q_{tB} = T_{fb} I_{cf} \tag{38}$$

$$Q_{tR} = T_r I_{cf} \tag{39}$$

$$Q_{krk} = T_{krk} I_{cf}^{1+GKRK} I_{kirk2}^{-GKRK} / (1 + GKRK) \tag{40}$$

$$I_{kirk2} = I_{krk}\left(1 - V_{BCike}/V_{krk}\right) \tag{41}$$

$$V_{BCike} = f\left(V_{BCi}, V_{ktr}, V_{kmx}\right) \tag{42}$$

$$f(x, y, z) = \frac{1}{2}\left[\sqrt{(x+z)^2 + y^2} + x - z\right] \tag{43}$$

$$Q_{tC} = \frac{1}{2}\left(Q_{tC1} + Q_{tC2} - Q_{tC3} Q_{tC4}\right) \tag{44}$$

$$Q_{tC1} = T_{fc0} I_{cf}\left[1 - V_{tc0}^{inv} f\left(V_{BCi}, V_{tr0}, V_{mx0}\right)\right] \tag{45}$$

$$Q_{tC2} = 2T_{cmin} I_{cf}\left[1 - V_{tcmin}^{inv} f\left(V_{BCi}, V_{trmin}, V_{mxmin}\right)\right] \tag{46}$$

$$Q_{tC3} = T_{fc0}\left[1 - V_{tc0}^{inv} f\left(V_{BCi}, V_{tr0}, V_{mx0}\right)\right] \tag{47}$$

$$Q_{tC4} = \sqrt{\left[I_{tc}\left(1 - V_{BCi} V_{tc}^{inv}\right) - I_{cf}\right]^2 + \left(I_{tc2}\right)^2} \tag{48}$$

The total extrinsic charges equal the corresponding extrinsic depletion charges, and the total intrinsic charges consist of both the depletion and diffusion components. The details are as follows [49]:

$$Q_{BCx} = ABCX\, Q_{BCd}(V_{BCx}) \tag{49}$$

$$Q_{BEx} = ABEX\, Q_{BEd}(V_{BEx}) \tag{50}$$

$$Q_{BCi} = (1 - ABCX)\, Q_{BCd}(V_{BCi}) + FEXTB Q_{tB} + FEXTC Q_{tC} + FEXKE Q_{krk} + Q_{tR} \tag{51}$$

TABLE 7. Model Parameters of the Charge Sources of the 1-Finger HBT.

C_{jBE}(fF)	V_{jBE}(V)	C_{BEmax}(fF)	V_{ptBE}(V)	M_{jBE}	M_{jBEr}
217.0	1.32	900.0	0.3	0.28	0.15
C_{jBC}(fF)	V_{jBC}(V)	C_{BCmax}(fF)	V_{ptBC}(V)	M_{jBC}	M_{jBCr}
113.0	0.8785	1054.7	2.0868	0.32	0.31
T_{fb}(ps)	T_{fc0}(ps)	T_{cmin}(ps)	I_{tc}(mA)	I_{tc2}(mA)	V_{tc0}^{inv}(V^{-1})
0.9	1.3672	0.79	28.2326	8.5	0.4183
V_{tr0}(V)	V_{mx0}(V)	V_{tcmin}^{inv}(V^{-1})	V_{trmin}(V)	V_{mxmin}(V)	V_{tc}^{inv}(V^{-1})
1.3	1.0	0.4	1.0	10.0	0.01516
T_{krk}(ps)	I_{krk}(mA)	I_{krktr}(μA)	V_{krk}(V)	*GKRK*	V_{ktr}(V)
1.5838	180	1.0	1.316	1.9	0.3
V_{kmx}(mV)	T_r(ns)	*ABEX*	*FEXTB*	*FEXTC*	*FEXKE*
-808.25	0.5	0.55	0.1	0.45	0.5

TABLE 8. Model Parameters of the Charge Sources of the 2-Finger HBT.

C_{jBE}(fF)	V_{jBE}(V)	C_{BEmax}(fF)	V_{ptBE}(V)	M_{jBE}	M_{jBEr}
431.0	1.29	1585.0	0.3	0.28	0.15
C_{jBC}(fF)	V_{jBC}(V)	C_{BCmax}(fF)	V_{ptBC}(V)	M_{jBC}	M_{jBCr}
178	0.8785	2109.4	2.55	0.35	0.2633
T_{fb}(ps)	T_{fc0}(ps)	T_{cmin}(ps)	I_{tc}(mA)	I_{tc2}(mA)	V_{tc0}^{inv}(V^{-1})
0.9	1.36717	0.84	51.0	19.0	0.41828
V_{tr0}(V)	V_{mx0}(V)	V_{tcmin}^{inv}(V^{-1})	V_{trmin}(V)	V_{mxmin}(V)	V_{tc}^{inv}(V^{-1})
1.3	1.0	0.41878	1.0	10.0	0.015155
T_{krk}(ps)	I_{krk}(mA)	I_{krktr}(μA)	V_{krk}(V)	*GKRK*	V_{ktr}(V)
1.5838	260.5	1.0	1.316	2.18	0.3
V_{kmx}(mV)	T_r(ns)	*ABEX*	*FEXTB*	*FEXTC*	*FEXKE*
-808.25	0.5	0.55	0.1	0.5	0.5

$$Q_{BEi} = (1 - ABEX)\, Q_{BEd}\,(V_{BEi}) + (1 - FEXTB)\, Q_{tB} + (1 - FEXTC)\, Q_{tC} + (1 - FEXKE)\, Q_{krk} \quad (52)$$

The determined parameters of the depletion and diffusion charge models for the 1-finger and 2-finger HBTs are listed in Tables 7 and 8, respectively.

IV. MODEL IMPLEMENTATION AND VERIFICATION

After all parameters are determined, the final large-signal models are built in ADS commercial software. The value ranges of the bias-emitter voltage variables are different at different temperatures, even though the bias conditions are totally the same [44]. Subsequently, the junction voltages are expanded by the first-order Taylor series, and another subcircuit is utilized to obtain the values of the junction voltages at 25°C (i.e. $\boldsymbol{V}\,(n)|_{n=n_1}$).

The nonlinear charge source, current source, and self-heating models are implemented by using Symbolically-Defined Devices (SDD) in ADS. Both implicit mode (53) and explicit mode (54) are utilized to define a nonlinear relationship of port voltages and port currents. In addition, a weighting function is used to scale the spectrum of a port current. For example, (54) illustrates the definition of the extrinsic base-collector current and charge. The SDD describes the model in terms of charges and currents, and it automatically generates the derivatives, which is similar to Verilog-A [50]. In addition, it is possible to translate these models into Verilog-A.

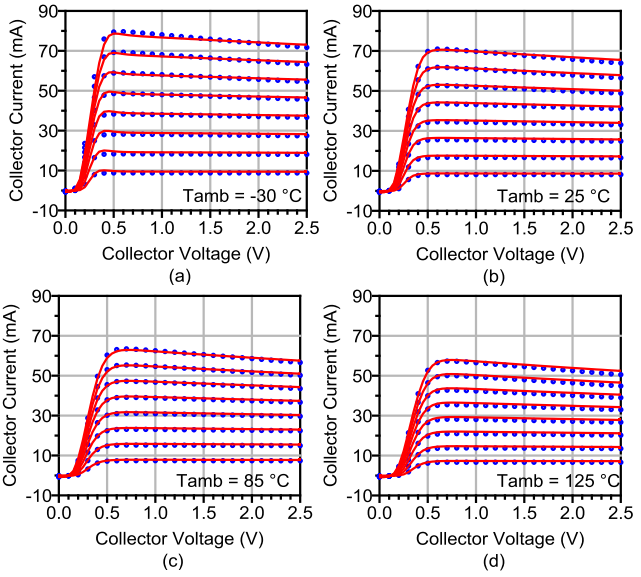

FIGURE 11. Measured (blue circles) and simulated (red solid lines) DC I-V characteristics by the 1-finger HBT large-signal model at different ambient temperature (a) $T_{amb} = -30°C$; (b) $T_{amb} = 25°C$; (c) $T_{amb} = 85°C$; (d) $T_{amb} = 125°C$. I_B increases from 100 μA to 800 μA in step of 100 μA and V_{CE} increases from 0 V to 2.5 V in increments of 50 mV.

The corresponding definitions in Verilog-A are given by (55) and (56).

$$\mathrm{F}[5, 0] = \_i5 - I_{CE} \quad (53)$$

$$\mathrm{I}[1] = \mathrm{I}[1, 0] + \mathrm{I}[1, 1] = I_{BCx} + \frac{dQ_{BCx}}{dt} \quad (54)$$

$$\mathrm{I}\,(ci, e) < +I_{CE} \quad (55)$$

$$\mathrm{I}\,(bx, cx) < +I_{BCx} + \mathrm{ddt}(Q_{BCx}) \quad (56)$$

where I_{CE} and I_{BCx} are constructed using (17)-(24).

Extensive comparisons between the simulated and measured results are made to validate the designed large-signal models and to verify the effectiveness of the adopted method. The constructed large-signal models manage to predict with great accuracy both small-signal and large-signal characteristics, including the I-V characteristics from −30°C to 125°C, multi-bias S-parameters from 0.1 GHz to 25.1 GHz at 25°C and 85°C, and large-signal characteristics from 4.9 GHz to 5.8 GHz at 25°C. Therefore, the design models are accurate, and the dimension reduction method is feasible and effective. In this work, the large-signal models are mainly used to help design power amplifiers. More measurements are needed if the models are used for some applications involving more severe operating conditions.

A. DC I-V CHARACTERISTICS

As shown in Fig. 11 and Fig. 12, the nonlinear models manage to predict the static current at four different ambient temperatures. Fig. 13 illustrates the measured and simulated input transfer characteristics. At a fixed ambient temperature, the self-heating effect leads to a decrease in the collector-emitter current with the increase of bias voltages.

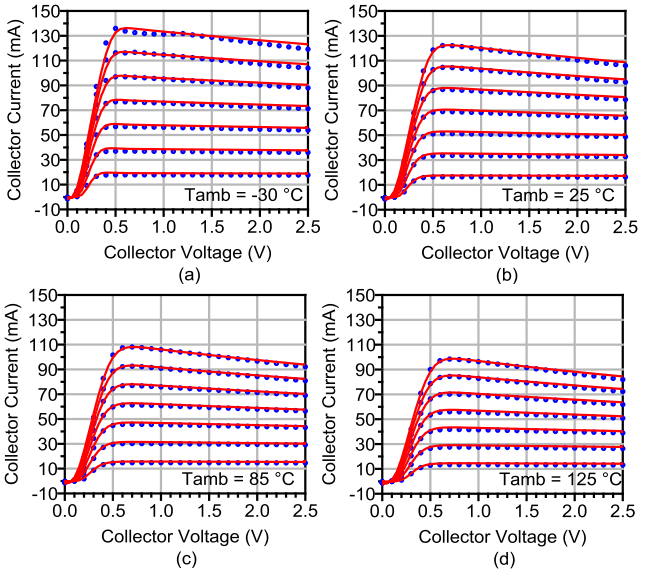

FIGURE 12. Measured (blue circles) and simulated (red solid lines) DC I-V characteristics by the 2-finger HBT large-signal model at different ambient temperature (a) $T_{amb} = -30°C$; (b) $T_{amb} = 25°C$; (c) $T_{amb} = 85°C$; (d) $T_{amb} = 125°C$. I_B increases from 200 μA to 1400 μA in step of 200 μA and V_{CE} increases from 0 V to 2.5 V in increments of 50 mV.

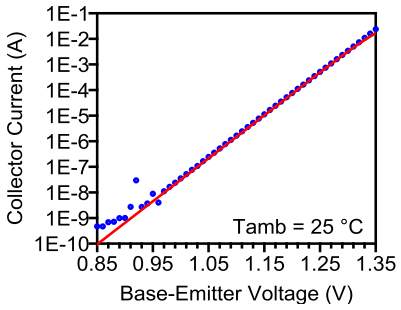

FIGURE 13. Measured (blue circles) and simulated (red solid lines) I_C with V_{BE} from 0.85 V to 1.35 V at room temperature.

The current collapse resulting from the self-heating effect is accurately modeled. Therefore, the adopted dimension reduction method is feasible and effective for the thermal modeling of semiconductor devices.

In fact, another expression of the static current source model is obtained by rearranging (25), which is given by

$$I_{DC}(\boldsymbol{m}, n) \approx [1 - 0.01(T_{amb} + P_{diss} \times R_{th} - 25)]\, I(\boldsymbol{m}, n_1) + 0.01(T_{amb} + P_{diss} \times R_{th} - 25) I(\boldsymbol{m}, n_2) \quad (57)$$

Equation (57) illustrates that the final current model with consideration of the self-heating effects is a linear combination of two independent sets of I-V expressions ($I(\boldsymbol{m}, n_1)$ and $I(\boldsymbol{m}, n_2)$). The percentage of each component is determined by the thermal state (T_{dev}). $I(\boldsymbol{m}, n_1)$ dominates the current in the low temperature or power dissipation region, whereas $I(\boldsymbol{m}, n_2)$ has an increasing influence on the current with the increase of the ambient temperature or the product of the thermal resistance and the average power dissipation.

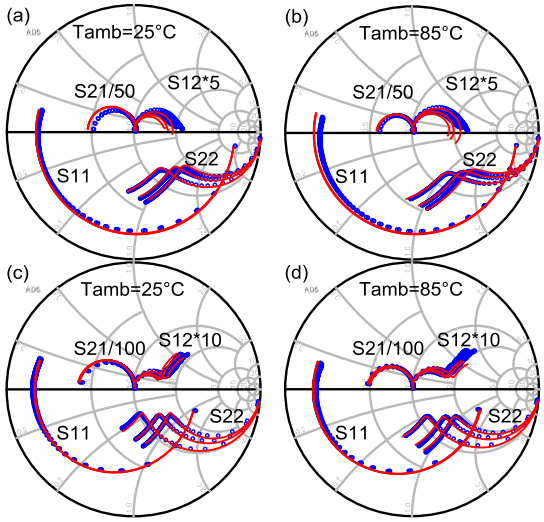

FIGURE 14. Comparison of the CW S-parameter measurements (blue circles) and simulations (solid lines) from 0.1 GHz to 25.1 GHz for the 1-finger HBT at (a) $I_B = 68$ μA, $T_{amb} = 25°C$; (b) $I_B = 68$ μA, $T_{amb} = 85°C$; (c) $I_B = 257$ μA, $T_{amb} = 25°C$; (d) $I_B = 257$ μA, $T_{amb} = 85°C$. V_{CE} increases from 2 V to 4 V in increments of 1 V.

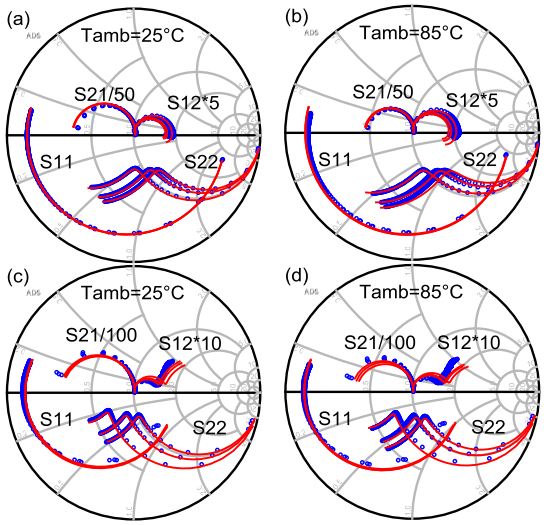

FIGURE 15. Comparison of the CW S-parameter measurements (blue circles) and simulations (solid lines) from 0.1 GHz to 25.1 GHz for the 2-finger HBT at (a) $I_B = 98$ μA, $T_{amb} = 25°C$; (b) $I_B = 98$ μA, $T_{amb} = 85°C$; (c) $I_B = 477$ μA, $T_{amb} = 25°C$; (d) $I_B = 477$ μA, $T_{amb} = 85°C$. V_{CE} increases from 2 V to 4 V in increments of 1 V.

B. SMALL SIGNAL CHARACTERISTICS

Fig. 14 and Fig. 15 show that the simulated constant wave S-parameters agree well with the measured results from 0.1 GHz to 25.1 GHz under different bias conditions. In addition, Fig. 16 shows the measured and simulated Y-parameters. The extrinsic and intrinsic parameters are accurately extracted, and the nonlinear current and charge sources are accurately modeled because the small-signal models are derived from the nonlinear current source and charge source. In addition, an excellent agreement is achieved between measurement and simulation at different ambient

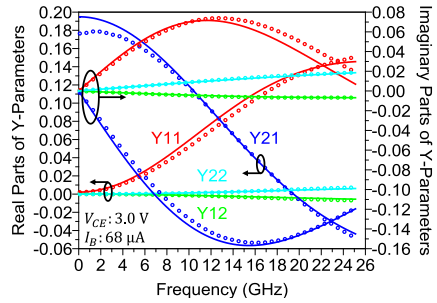

FIGURE 16. Comparison of the Y-parameter measurements (circles) and simulations (solid lines) from 0.1 GHz to 25.1 GHz for the 1-finger HBT at $I_B = 68\ \mu A$, $V_{CE} = 3$ V, and $T_{amb} = 25°C$.

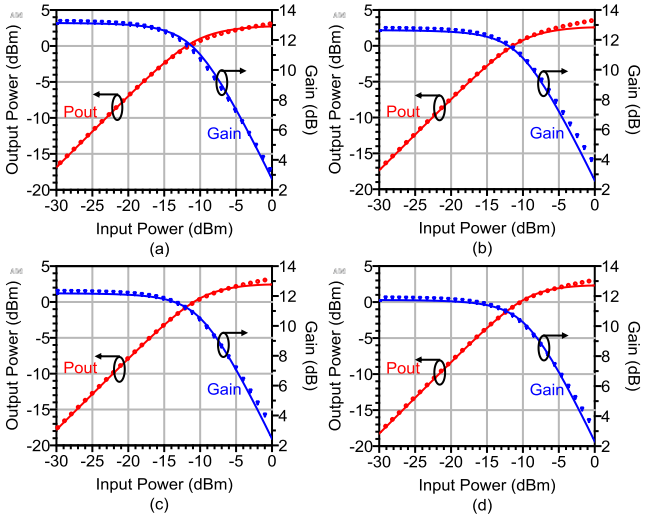

FIGURE 17. Comparison of the measured (symbols) and simulated results (solid lines) of the output power and gain for the 1-finger HBT at different frequencies (a) 4.9 GHz; (b) 5.2 GHz; (c) 5.5 GHz; (d) 5.8 GHz. I_B is 68 μA and V_{CE} is 3.3 V. The ambient temperature is 25°C.

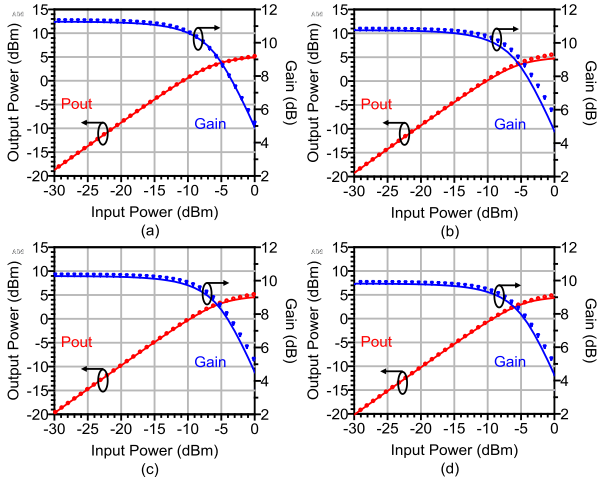

FIGURE 18. Comparison of the measured (symbols) and simulated results (solid lines) of the output power and gain for the 2-finger HBT at different frequencies (a) 4.9 GHz; (b) 5.2 GHz; (c) 5.5GHz; (d) 5.8 GHz. I_B is 98 μA and V_{CE} is 3.3 V. The ambient temperature is 25°C.

temperatures. Therefore, the thermal effects on the collector current are successfully captured by using the dimension reduction method.

C. LARGE-SIGNAL CHARACTERISTICS

Fig. 17 and Fig. 18 demonstrate the power sweep validation of the 1-finger and 2-finger HBT models at room temperature. The source and load impedances are 50 ohms. The constructed models manage to predict with great accuracy the output power and gain compression from 4.9 GHz to 5.8 GHz. The good agreement between the simulation and measurement verifies the designed nonlinear models with consideration of thermal effects and validates the effectiveness of the dimension reduction method.

V. CONCLUSION

In conclusion, the dimension reduction method is utilized in this paper for the quick and accurate thermal modeling of InGaP/GaAs HBTs. Empirical functions are used to describe the relationship between currents and junction voltages, whereas the Taylor series is used to represent the temperature dimension. The large-signal model is implemented in ADS commercial software. A good agreement is achieved between simulation and measurement under different bias and temperature conditions, including pulsed I-V, DC I-V, S-parameters, and power sweeps. The number of temperature scaling equations and related parameters is successfully reduced by using the dimension reduction method. In addition, this method can be effectively applied for the thermal modeling of various devices based on different materials or process technologies, including LDMOS, diodes, and so on. Therefore, the design time could be significantly shortened, and the automatic extraction and modeling could be realized.

APPENDIX

If the N-order Taylor series expansion is applied, the number of the coefficients (i.e., the Jacobian $\nabla I(\boldsymbol{m}, n)|_{n=n_1}$, Hessian $\mathrm{H}I(\boldsymbol{m}, n)|_{n=n_1}$, etc.) to be determined is N. For convenience, these coefficients are denoted as $J_1, J_2, \ldots, J_N$. Then, the current is approximately expressed by

$$I(\boldsymbol{m}, n) \approx I(\boldsymbol{m}, n)|_{n=n_1} + \frac{(n-n_1)}{1!} \cdot J_1 + \frac{(n-n_1)^2}{2!} \cdot J_2 + \cdots + \frac{(n-n_1)^N}{N!} \cdot J_N \quad (58)$$

where $\boldsymbol{m} = (V_{BCx}, V_{BCi}, V_{BEx}, V_{BEi})$ and $n = T_{dev}$. n_1 is the quiescent expansion point.

In fact, the number of reference states would increase with the order of approximation, and thus more measurement date and curve fitting at different states are needed. However, it is still convenient to determine the coefficients and model parameters if the order of approximation is not extremely high. All the coefficients in (58) have the dimension of 1-by-1 because only the temperature dimension is expanded. Therefore, at least N+1 different states are required to determine the expression of these coefficients. If the pulsed I-V measurements at N+1 different thermal states are used for determination, for $k = 2, 3, \cdots, N+1$,

the current is expressed as follows:

$$I(\boldsymbol{m}, n_k) \approx I(\boldsymbol{m}, n_1) + \frac{(n_k - n_1)}{1!} \cdot J_1 + \frac{(n_k - n_1)^2}{2!} \cdot J_2 + \cdots + \frac{(n_k - n_1)^N}{N!} \cdot J_N \quad (59)$$

Rearranging (59) in vector form, we obtain

$$\boldsymbol{A} \cdot \left[J_1 \; J_2 \; \ldots \; J_N \right]^T = \boldsymbol{b} \quad (60)$$

where the matrix $\boldsymbol{A}$ has the dimension of N-by-N and the vector $\boldsymbol{b}$ has N components. The expressions are as follows:

$$\boldsymbol{A} = \begin{bmatrix} (n_2 - n_1) & \cdots & \frac{1}{N!}(n_2 - n_1)^N \\ \vdots & \ddots & \vdots \\ (n_{N+1} - n_1) & \cdots & \frac{1}{N!}(n_{N+1} - n_1)^N \end{bmatrix} \quad (61)$$

$$\boldsymbol{b} = \begin{bmatrix} I(\boldsymbol{m}, n_2) - I(\boldsymbol{m}, n_1) \\ \vdots \\ I(\boldsymbol{m}, n_{N+1}) - I(\boldsymbol{m}, n_1) \end{bmatrix} \quad (62)$$

Then, since the number of the equations is the same as the number of the variables, the coefficients can be quickly and uniquely obtained by

$$\left[J_1 \; J_2 \; \ldots \; J_N \right] = \left[\boldsymbol{A}^{-1} \cdot \boldsymbol{b} \right]^T \quad (63)$$

Similarly, the model parameters (i.e., parameters in $I(\boldsymbol{m}, n_1), I(\boldsymbol{m}, n_2), \cdots, I(\boldsymbol{m}, n_{N+1})$) can be quickly obtained by using the Plot Optimizer in IC-CAP software. Hence, if the order of approximation is not extremely high, it is still convenient to extract the coefficients and parameters. It would be better to determine individual thermal coefficients if the order of approximation is very high, but the first- or second-order expansion is generally enough for most applications.

REFERENCES

[1] I. Ammar, A. B. Kouki, and F. M. Ghannouchi, "A simple large signal model for III–V HBT devices exceeding VBIC performances," *AEU Int. J. Electron. Commun.*, vol. 60, no. 5, pp. 367–375, May 2006.
[2] H. Bo, L. Shoulin, C. Jiali, Y. Qiuyan, and G. Jianjun, "MEXTRAM model based SiGe HBT large-signal modeling," *J. Semicond.*, vol. 31, no. 10, Oct. 2010, Art. no. 104004.
[3] B. Li, S. Prasad, L.-W. Yang, and S. C. Wang, "A semianalytical parameter-extraction procedure for HBT equivalent circuit," *IEEE Trans. Microw. Theory Techn.*, vol. 46, no. 10, pp. 1427–1435, Oct. 1998.
[4] G. He, J. Howard, M. Le, P. Partyka, B. Li, G. Kim, R. Hess, R. Bryie, R. Lee, S. Rustomji, J. Pepper, M. Kail, M. Helix, R. B. Elder, D. S. Jansen, N. E. Harff, J. F. Prairie, E. S. Daniel, and B. K. Gilbert, "Self-aligned InP DHBT with f_T and f_{max} over 300 GHz in a new manufacturable technology," *IEEE Electron Device Lett.*, vol. 25, no. 8, pp. 520–522, Aug. 2004.
[5] A. Samelis and D. Pavlidis, "DC to high-frequency HBT-model parameter evaluation using impedance block conditioned optimization," *IEEE Trans. Microw. Theory Techn.*, vol. 45, no. 6, pp. 886–897, Jun. 1997.
[6] M. Hafizi, C. R. Crowell, and M. E. Grupen, "The DC characteristics of GaAs/AlGaAs heterojunction bipolar transistors with application to device modeling," *IEEE Trans. Electron Devices*, vol. 37, no. 10, pp. 2121–2129, Oct. 1990.
[7] K. Lu, P. A. Perry, and T. J. Brazil, "A new large-signal AlGaAs/GaAs HBT model including self-heating effects, with corresponding parameter-extraction procedure," *IEEE Trans. Microw. Theory Techn.*, vol. 43, no. 7, pp. 1433–1445, Jul. 1995.
[8] M. Rudolph, R. Doerner, K. Beilenhoff, and P. Heymann, "Scalable GaInP/GaAs HBT large-signal model," *IEEE Trans. Microw. Theory Techn.*, vol. 48, no. 12, pp. 2370–2376, Dec. 2000.
[9] F. X. Sinnesbichler and G. R. Olbrich, "Accurate large-signal modeling of SiGe HBTs," in *IEEE MTT-S Int. Microw. Symp. Dig.*, Boston, MA, USA, Jun. 2000, pp. 749–752.
[10] A. Raghavan, S. Venkataraman, B. Banerjee, Y. Suh, D. Heo, and J. Laskar, "Direct extraction of an empirical temperature-dependent InGaP/GaAs HBT large-signal model," *IEEE J. Solid-State Circuits*, vol. 38, no. 9, pp. 1443–1450, Sep. 2003.
[11] M. Tutt, "GaAs based HBT large signal modeling using VBIC for linear power amplifier applications," in *Proc. BIPOLAR/BiCMOS Circuits Technol. Meeting*, Minneapolis, MN, USA, Sep. 2000, pp. 58–61.
[12] P. C. Grossman and C. John, "Large signal modeling of HBT's including self-heating and transit time effects," *IEEE Trans. Microw. Theory Tech.*, vol. 40, no. 3, pp. 449–464, Mar. 1992.
[13] T.-Y. Lee, S. Lee, P. Zampardi, and J. Kang, "Large-signal modeling of SiGe HBT for PA applications," in *Proc. IEEE Bipolar/BiCMOS Circuits Technol. Meeting (BCTM)*, Austin, TX, USA, Oct. 2010, pp. 94–97.
[14] Z. Wen, Y. Xu, Y. Chen, H. Tao, C. Ren, H. Lu, Z. Wang, W. Zheng, B. Zhang, T. Chen, T. Gao, and R. Xu, "A quasi-physical compact large-signal model for AlGaN/GaN HEMTs," *IEEE Trans. Microw. Theory Techn.*, vol. 65, no. 12, pp. 5113–5122, Dec. 2017.
[15] Y. Fu, R. Xu, J. Zhou, X. Yu, Z. Wen, Y. Kong, T. Chen, Y. Zhang, B. Yan, J. He, and Y. Xu, "A large-signal model for two-dimensional hole gas diamond MOSFET based on the QPZD," *IEEE Access*, vol. 7, pp. 76868–76877, 2019.
[16] A. Huang, Z. Zhong, Y.-X. Guo, and W. Wu, "A dimension-reduced artificial neural network for the compact modeling of semiconductor devices," in *IEEE MTT-S Int. Microw. Symp. Dig. (IWS)*, Chengdu, China, May 2018, pp. 1–4.
[17] A. Huang, Z. Zhong, Y. Guo, and W. Wu, "A temperature dependent empirical model for AlGaN/GaN HEMTs including charge trapping and self-heating effects," in *IEEE MTT-S Int. Microw. Symp. Dig. (IMS)*, Honolulu, HI, USA, Jun. 2017, pp. 248–251.
[18] A.-D. Huang, Z. Zhong, Y.-X. Guo, and W. Wu, "A general dimension reduction method for the dispersion modeling of semiconductor devices," *IEEE Access*, vol. 6, pp. 39422–39434, 2018.
[19] S. J. Spiegel, D. Ritter, R. A. Hamm, A. Feygenson, and P. R. Smith, "Extraction of the InP/GaInAs heterojunction bipolar transistor small-signal equivalent circuit," *IEEE Trans. Electron Devices*, vol. 42, no. 6, pp. 1059–1064, Jun. 1995.
[20] U. Schaper and B. Holzapfl, "Analytical parameter extraction of the HBT equivalent circuit with T-like topology from measured S-parameters," *IEEE Trans. Microw. Theory Techn.*, vol. 43, no. 3, pp. 493–498, Mar. 1995.
[21] S. A. Maas and D. Tait, "Parameter-extraction method for heterojunction bipolar transistors," *IEEE Microw. Guided Wave Lett. (until 2002)*, vol. 2, no. 12, pp. 502–504, Dec. 1992.
[22] J. B. Scott, "New method to measure emitter resistance of heterojunction bipolar transistors," *IEEE Trans. Electron Devices*, vol. 50, no. 9, pp. 1970–1973, Sep. 2003.
[23] J. Gao, "Small-Signal Modeling and Parameter Extraction of HBT," in *Heterojunction Bipolar Transistors for Circuit Design: Microwave Modeling and Parameter Extraction*, 1st ed. Singapore: Wiley, 2015, pp. 117–154.
[24] J. Gao, X. Li, H. Wang, and G. Boeck, "Approach for determination of extrinsic resistance for equivalent circuit model of metamorphic InP/InGaAs HBTs," *IEE Proc. Microw., Antennas Propag.*, vol. 152, no. 3, pp. 195–200, Jun. 2005.
[25] J. Gao, X. Li, H. Wang, and G. Boeck, "An approach to determine small-signal model parameters for InP-based heterojunction bipolar transistors," *IEEE Trans. Semicond. Manuf.*, vol. 19, no. 1, pp. 138–145, Feb. 2006.
[26] M. Sotoodeh, L. Sozzi, A. Vinay, A. H. Khalid, Z. Hu, A. A. Rezazadeh, and R. Menozzi,"Stepping toward standard methods of small-signal parameter extraction for HBTs," *IEEE Trans. Electron Devices*, vol. 47, no. 6, pp. 1139–1151, Jun. 2000.
[27] B. Li and S. Prasad, "Basic expressions and approximations in small-signal parameter extraction for HBT's," *IEEE Trans. Microw. Theory Techn.*, vol. 47, no. 5, pp. 534–539, May 1999.
[28] F. Stein, D. Celi, C. Maneux, N. Derrier, and P. Chevalier, "Robustness of the base resistance extraction method for SiGe HBT devices," in in *Proc. Int. Semiconductor Conf. Dresden Grenoble (ISCDG)*, Sep. 2013, pp. 1–4.

[29] W. B. Tang, C. M. Wang, and Y. M. Hsin, "A new extraction technique for the complete small-signal equivalent-circuit model of InGaP/GaAs HBT including base contact impedance and AC current crowding effect," *IEEE Trans. Microw. Theory Techn.*, vol. 54, no. 10, pp. 3641–3647, Oct. 2006.

[30] O. Sevimli, A. E. Parker, A. P. Fattorini, and S. J. Mahon, "Measurement and modeling of thermal behavior in InGaP/GaAs HBTs," *IEEE Trans. Electron Devices*, vol. 60, no. 5, pp. 1632–1639, May 2013.

[31] H. K. Gummel and H. C. Poon, "An integral charge control model of bipolar transistors," *Bell Syst. Tech. J.*, vol. 49, no. 5, pp. 827–852, May 1970.

[32] I. Angelov, K. Choumei, and A. Inoue, "An empirical HBT large-signal model for CAD," in *IEEE MTT-S Int. Microw. Symp. Dig. (IMS)*, Seattle, WA, USA, Jun. 2002, pp. 518–533.

[33] J. Mcmacken, S. Nedeljkovic, J. Gering, and D. Halchin, "HBT modeling," *IEEE Microw. Mag.*, vol. 9, no. 2, pp. 48–71, Apr. 2008.

[34] L. H. Camnitz, S. Kofol, T. Low, and S. R. Bahl, "An accurate, large signal, high frequency model for GaAs HBTs," in *GaAs IC Symp. IEEE Gallium Arsenide Integr. Circuit Symp. 18th Annu. Tech. Dig.*,. Orlando, FL, USA, Nov. 1996, pp. 303–306.

[35] M. Rudolph, C. Fager, and D. E. Root, *Nonlinear Transistor Model Parameter Extraction Techniques*. New York, NY, USA: Cambridge Univ. Press, 2011.

[36] C. C. McAndrew, J. A. Seitchik, D. F. Bowers, M. Dunn, M. Foisy, I. Getreu, M. McSwain, S. Moinian, J. Parker, D. J. Roulston, M. Schroter, P. van Wijnen, and L. F. Wagner, "VBIC95, the vertical bipolar inter-company model," *IEEE J. Solid-State Circuits*, vol. 31, no. 10, pp. 1476–1483, Oct. 1996.

[37] R. Menozzi, J. Barrett, and P. Ersland, "A new method to extract HBT thermal resistance and its temperature and power dependence," *IEEE Trans. Device Mater. Rel.*, vol. 5, no. 3, pp. 595–601, Sep. 2005.

[38] A. Issaoun, F. M. Ghannouchi, and A. B. Kouki, "An accurate and compact large signal model for III–V HBT devices," *Solid-state Electron.*, vol. 49, no. 12, pp. 1909–1916, Dec. 2005.

[39] N. Bovolon, P. Baureis, J.-E. Müller, P. Zwicknagl, R. Schultheis, and E. Zanoni, "A simple method for the thermal resistance measurement of AlGaAs/GaAs heterojunction bipolar transistors," *IEEE Trans. Electron Devices*, vol. 45, no. 8, pp. 1846–1848, Aug. 1998.

[40] A. M. Darwish, A. J. Bayba, A. Khorshid, A. Rajaie, and H. A. Hung, "Calculation of the nonlinear junction temperature for semiconductor devices using linear temperature values," *IEEE Trans. Electron Devices*, vol. 59, no. 8, pp. 2123–2128, Aug. 2012.

[41] C. P. Baylis, L. P. Dunleavy, and J. E. Daniel, "Direct measurement of thermal circuit parameters using pulsed IV and the normalized difference unit," in *IEEE MTT-S Int. Microw. Symp. Dig.*, vol. 2, Jun. 2004, pp. 1231–1234.

[42] B. Han, T. Zhou, X. Xu, P. Li, and J. Gao, "Scalable large-signal model for SiGe HBTs," *Int. J. RF Microw. Comput. Eng.*, vol. 22, no. 2, pp. 175–183, Mar. 2012.

[43] A. Zhang and J. Gao, "Emitter-length scalable small signal and noise modeling for InP heterojunction bipolar transistors," *IEEE Access*, vol. 7, pp. 13939–13944, 2019.

[44] S. R. Nedeljkovic, J. R. McMacken, P. J. Partyka, and J. M. Gering, "A custom III–V heterojunction bipolar transistor model," *Microw. J. Int. Ed*, vol. 52, no. 4, pp. 60–84, Apr. 2009.

[45] M. Schroter and T.-Y. Lee, "Physics-based minority charge and transit time modeling for bipolar transistors," *IEEE Trans. Electron Devices*, vol. 46, no. 2, pp. 288–300, Feb. 1999.

[46] J. J. Liou, L. L. Liou, C. I. Huang, and B. Bayraktaroglu, "A physics-based, analytical heterojunction bipolar transistor model, including thermal and high-current effects," *IEEE Trans. Electron Devices*, vol. 40, no. 9, pp. 1570–1577, Sep. 1993.

[47] C. Yuxiong, J. Zhi, G. Ji, S. Yongbo, and L. Xinyu, "A symbolically defined InP double heterojunction bipolar transistor large-signal model," *J. Semicond.*, vol. 30, no. 12, pp. 37–41, Dec. 2009.

[48] M. S. Shirokov, S. V. Cherepko, X. Du, J. C. M. Kwang, and D. A. Teeter, "Large-signal modeling and characterization of high-current effects in InGaP/GaAs HBTs," *IEEE Trans. Microw. Theory Techn.*, vol. 50, no. 4, pp. 1084–1094, Apr. 2002.

[49] M. Iwamoto, D. E. Root, J. B. Scott, A. Cognata, P. M. Asbeck, B. Hughes, and D. C. D'Avanzo, "Large-signal HBT model with improved collector transit time formulation for GaAs and InP technologies," in *IEEE MTT-S Int. Microw. Symp. Dig. (IMS)*, Philadelphia, PA, USA, Jun. 2003, pp. 635–638.

[50] (Aug. 12, 2005). *Using Verilog-A in Advanced Design System, Agilent Technologies*, Palo Alto, CA, USA, Accessed: Sep. 15, 2019. [Online]. Available: http://literature.cdn.keysight.com/litweb/pdf/ads2005a/pdf/veriloga.pdf

WENRUI HU received the B.Eng. degree in communication engineering from the Nanjing University of Science and Technology, Nanjing, China, in 2017, and the M.Sc. degree from the National University of Singapore, Singapore, in 2018, where he is currently pursuing the Ph.D. degree in electrical engineering. His current research interest includes RF/microwave semiconductor device modeling and characterization.

ANDONG HUANG was born in Jiangxi, China, in 1991. He received the B.S. and Ph.D. degrees from the Department of Optoelectronic Technology, Nanjing University of Science and Technology, Nanjing, China, in 2013 and 2019, respectively. In 2013, he was an Exchange Student with the Institute for Nanoelectronics, Technical University of Munich, Germany, where he conducted his final year project on locating stochastic signal sources. He was with the Department of Electrical and Computer Engineering, National University of Singapore, from 2014 to 2017, as a Visiting Ph.D. Student. His main research interests include semiconductor physics, RF/microwave semiconductor device modeling and characterization, microwave system modeling, EDA tool development, and near- or far-field wireless power transfer systems.

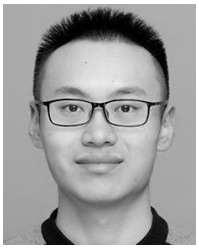

HAORUI LUO was born in Sichuan, China, in 1996. He received the B.Eng. degree from the School of Electronic and Optical Engineering, Nanjing University of Science and Technology, China, in 2018, and the M.Sc. degree from the National University of Singapore, Singapore, in 2019. His current research interest includes RF/microwave semiconductor device modeling and characterization.

YONG-XIN GUO (M'03–SM'05–F'18) received the B.Eng. and M.Eng. degrees from the Nanjing University of Science and Technology, Nanjing, China, and the Ph.D. degree from the City University of Hong Kong, in 1992, 1995, and 2001, respectively, all in electronic engineering.

He is currently a Full Professor with the Department of Electrical and Computer Engineering, National University of Singapore (NUS). He is also the Director of the Center of Advanced Microelectronic Devices, NUS Suzhou Research Institute. He has authored or coauthored over 430 international journal and conference papers and three book chapters. Thus far, his publications have been cited more than 8700 times and the H-index is 49 (source: Google Scholar). He holds two granted U.S. patents, two granted Chinese patents, and over ten filed patents in China. He has graduated 13 Ph.D. students at NUS. His current research interests include antennas, wireless power, RF and millimeter-wave sensing, and MMIC modeling and design for wireless communications, the IoTs, and biomedical applications.

Dr. Guo was a recipient of the Young Investigator Award 2009 from NUS. He received the 2013 Raj Mittra Travel Grant Senior Researcher Award. He is the Chair of the IEEE AP-S Technical Committee on Antenna Measurement, in 2018/2019. He has served as the General Chair/Co-Chair for APMC 2019, AWPT 2017, ACES-China 2017, the IEEE MTT-S IMWS-AMP 2015, and the IEEE MTT-S IMWS-Bio 2013. He has served as the Technical Program Committee (TPC) Co-Chair for the IEEE IMWS-AMP 2017/2019 and RFIT2009. He is serving as an Associate Editor for the IEEE JOURNAL OF ELECTROMAGNETICS, RFAND MICROWAVE IN MEDICINE AND BIOLOGY, the *IEEE Antennas and Propagation Magazine*, and *Electronics Letters*.